



HAL
open science

Observation of free oscillations after the 2010 Chile and 2011 Japan earthquakes by superconducting gravimeter in Kutch, Gujarat, India

Chandra Sekhar Pedapudi, Madhusudhana Rao Katlamudi, Séverine Rosat

► **To cite this version:**

Chandra Sekhar Pedapudi, Madhusudhana Rao Katlamudi, Séverine Rosat. Observation of free oscillations after the 2010 Chile and 2011 Japan earthquakes by superconducting gravimeter in Kutch, Gujarat, India. *Geodesy and Geodynamics*, 2022, 10.1016/j.geog.2022.10.002 . hal-03874434

HAL Id: hal-03874434

<https://hal.science/hal-03874434v1>

Submitted on 28 Nov 2022

HAL is a multi-disciplinary open access archive for the deposit and dissemination of scientific research documents, whether they are published or not. The documents may come from teaching and research institutions in France or abroad, or from public or private research centers.

L'archive ouverte pluridisciplinaire **HAL**, est destinée au dépôt et à la diffusion de documents scientifiques de niveau recherche, publiés ou non, émanant des établissements d'enseignement et de recherche français ou étrangers, des laboratoires publics ou privés.

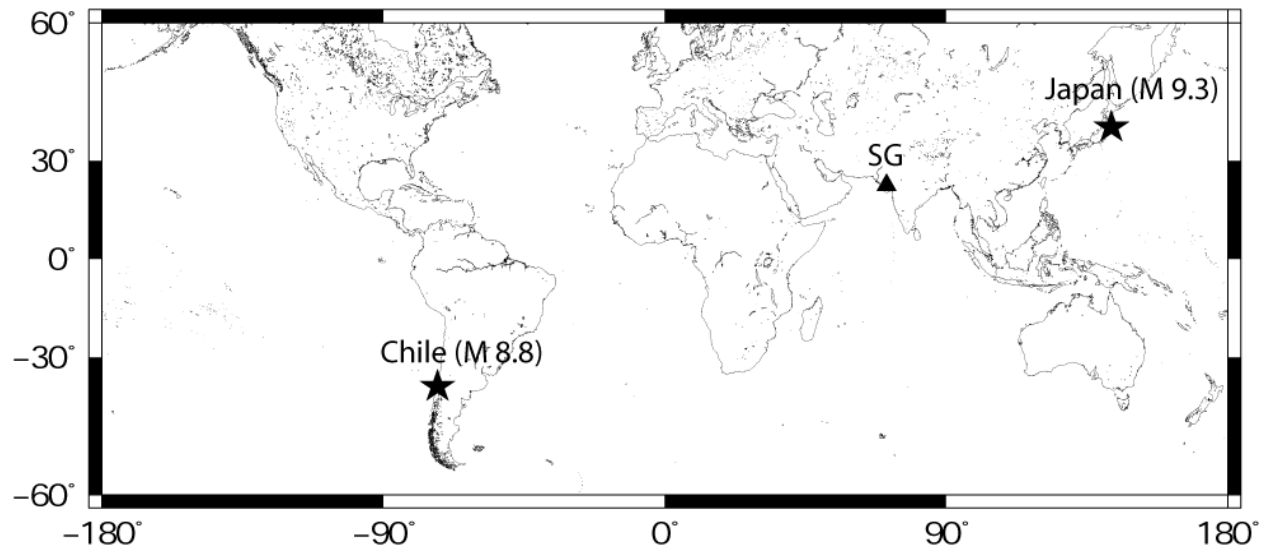
39 **1. Introduction**

40 In times of major earthquakes, volcanic eruptions or underground nuclear explosions, Earth free
41 oscillations (EFO) are generated in addition to seismic waves such as body and surface waves
42 [1]. Based on wave motion, free oscillations are mainly divided into two categories, namely
43 spheroidal oscillations and toroidal oscillations [2]. In the case of spheroidal oscillations, the
44 displacements are both radial and tangential, which can be described by the spherical harmonic
45 functions. As for the toroidal oscillations, the displacements are purely tangential. In the past, the
46 time series of very long period broadband seismographs were widely used to determine the
47 frequency, phase and decay factor of various EFO [3]. Identification of EFO is also done using
48 data of strainmeter and spring gravimeter [4]. Superconducting gravimeters (SGs) have the best
49 precision and sensitivity compared to other instruments, making them excellent tools for
50 characterizing the Earth's free oscillations [5, 6]. The SG can record normal modes between
51 periods of 10 s to 54 minutes [7, 8]. SG is a type of instrument that can measure the vertical
52 deformation of the Earth's surface and changes in the Earth's gravitational field over periods
53 ranging from seconds to years, including normal modes, Earth tides and other phenomena, with a
54 sampling rate of 1 or 2 seconds. SGs better characterize low-frequency seismic modes because
55 their response to atmospheric pressure changes is linear at low frequencies and can be better
56 reduced [9]. Benioff et al. [10] first identified the EFO mode using strain gauge data during the
57 Kamchatka earthquake (M~9) in 1952, which is a spheroidal mode with a period of 57 minutes.
58 Later, they found dozens of spheroidal free oscillations and toroidal modes using data from the
59 1960 Chilean earthquake. Besides large earthquakes, Tanimoto [11] and Nishida [12] report
60 continuous free oscillations of the fundamental modes between frequencies of 0.3 and 5 mHz.

61 The deviations of the observed frequencies of the normal modes from their theoretical values are
62 used to provide a measure of the deviation from the Earth's spherical symmetry including lateral
63 heterogeneities, while the EFO attenuation provides a measure of internal inelasticity. In fact,
64 seismic mode frequencies and damping factors were used to create the Preliminary Reference
65 Earth Model (PREM), which is still widely used in seismology and beyond [13]. Observing the
66 EFO gives us the opportunity to study the structure of the Earth's interior [14]. In the upper
67 mantle, some modes are sensitive to compressional velocities while others in the lower mantle
68 are sensitive to shear velocities [15, 16, 17]. By observing the EFO, we can also determine the
69 magnitude, duration and amplitude of the earthquake that produces the EFO [18]. We can also

70 study the solutions of the focal mechanism of large earthquakes using the observed EFO [18, 19,
71 20].

72 Institute of Seismological Research has established the Multi-Parameter Geophysical
73 Observatory at Badargadh (23.47°N, 70.62°E), Kutch, Gujarat, India to study earthquake
74 precursors in an integrated manner. Eleven different types of parameters are monitored using
75 instruments, namely Overhauser magnetometer, three-axis fluxgate magnetometer, induction coil
76 magnetometer, DI Flux magnetometer, radon in soil monitor, radon in water, SG, water level
77 recorder, differential GPS receiver, strong motion accelerometer and broadband seismometer.
78 High-precision devices have the sensitivity to detect characteristic disturbances caused by
79 tectonic activity near monitoring stations. The main objective of SG is to monitor the minute
80 fluctuations (at the sub-microgal scale, where $1 \mu\text{Gal} = 10 \text{ nm/s}^2$) of the Earth's gravitational
81 field due to small tectonic deformations and/or mass redistributions associated with the collision
82 between Indian plate and Asian plate, and to study co-seismic/precursory gravitational signals, if
83 any, to a large earthquake [22]. Arora et al. [23] reported the first observations of earth free
84 oscillations during the April 1, 2007 Solomon Islands earthquake ($M_S=8.1$) by Indian
85 superconducting gravimeter in the Himalayan region. Two strong earthquakes have occurred in
86 the last decade, namely the Tohoku earthquake of March 11, 2011 ($M_w 9.1$), which struck Japan
87 (according to USGS data) with a focal depth of 29 km, and the earthquake in Chile on February
88 27, 2010 ($M_w 8.8$) with a focal depth of 23 km. The epicenters of earthquakes in Chile and Japan
89 and the position of SG at Badargadh station are shown in Fig. 1. In this paper, we have examined
90 all EFO modes of these two strong earthquakes using data recorded with a superconducting
91 gravimeter in Badargadh, Gujarat, India and the observed free oscillations are compared with the
92 PREM model [13].



93
 94 **Figure 1:** Location map of Both the Japan and Chile earthquakes Epicenters and the Super
 95 Conducting Gravimeter at Badargadh MPMO Station.

96
 97 **2. Data and Method**

98 A superconducting gravimeter (SG) was installed in March 2009 in Badargadh, Gujarat, India
 99 and continuously records gravitational fluctuations at 1 sample/second (Hz). SGs are known to
 100 accurately measure the time-varying gravitational field with unprecedented resolution and
 101 temporal stability. Such an accurate and stable temporal gravity record gives us a unique
 102 opportunity to monitor and study a wide range of studies, from long-period tides to seismic
 103 normal modes [24]. By replacing the mechanical spring with the levitation of a magnetically
 104 suspended proof mass, the superconducting gravimeter solves the problem of erratic drift caused
 105 by relative gravimeters and seismometers in well-regulated environments [25]. The magnetic
 106 shield, the field coils and the levitating mass (sphere) are the three main superconducting
 107 elements of the SG [26]. The website (www.gwrinstruments.com) contains complete principles
 108 of operation for each of the elements of the superconducting gravimeter. The actual image of the
 109 superconducting gravimeter installed in Badargadh is shown in Fig2. The superconducting
 110 gravimeter we used is a two-sphere superconducting gravimeter, which increases data quality
 111 and has high consistency in drift tracking for better data resolution [27].

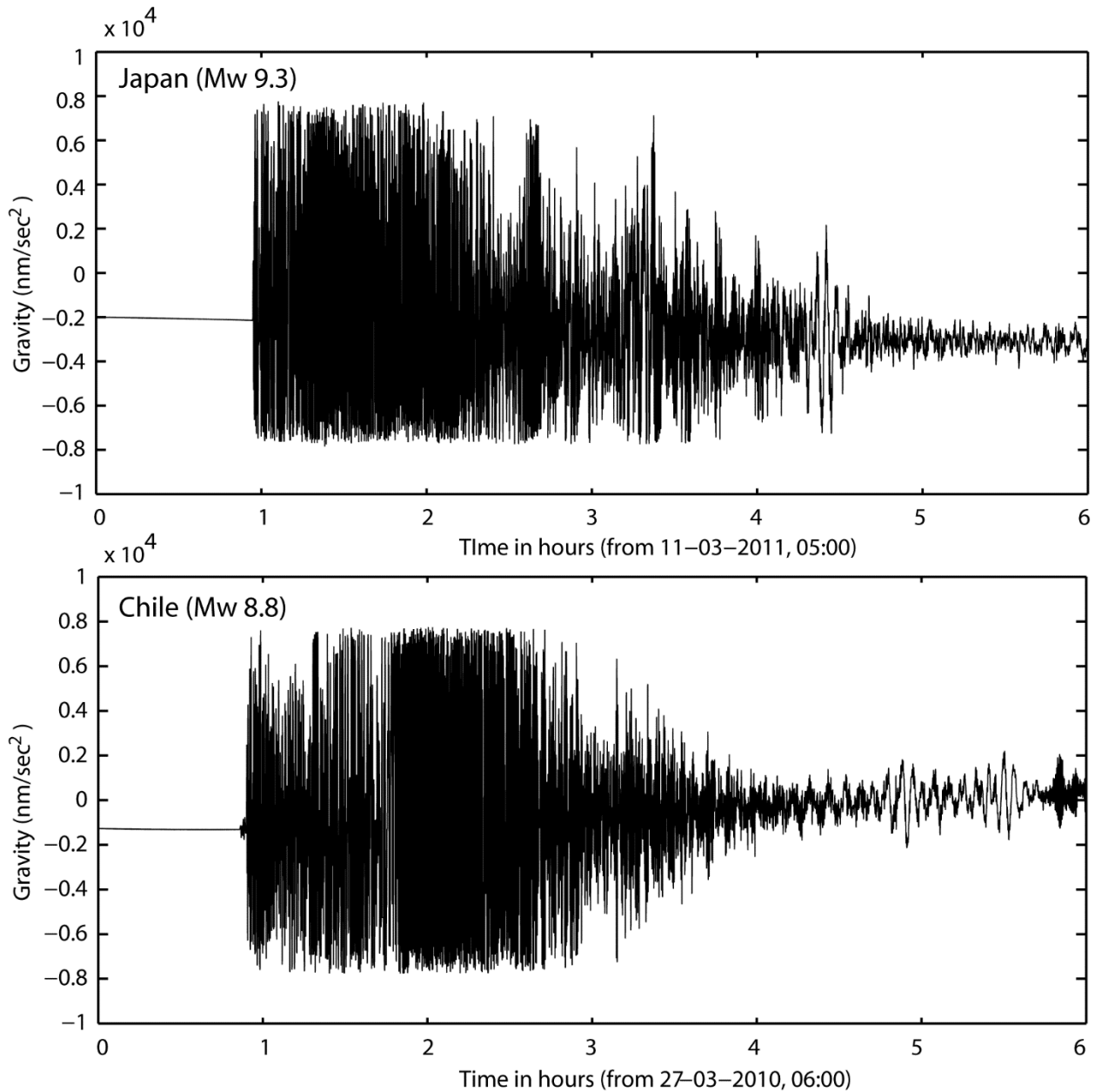


112

113 **Figure 2:** Superconducting Gravimeter placed in Badargadh station, Gujarat, India, a) DAC unit,
114 b) Dewar and c) the dome structure

115 In our study, we collected gravitational data for two major earthquakes in Japan on March 11,
116 2011 and the Chile earthquake on February 27, 2010. For the identification of free oscillations,
117 we used SG data spanning nearly 20 days (480 hours) after the occurrence of the respective
118 earthquakes, and these data are subject to pre-processing using TSoft software [28] such as:
119 removal of gravity tides, atmospheric pressure correction and spectral analysis of residual gravity
120 data [29]. After removing the solid earth tides generated by the WDD model [30] from the raw
121 data using TSoft, we then apply the 20-class fragmented polynomial fitting technique to remove
122 the remaining gravitational tides. For the fragmental polynomial fit, the best transit time is about
123 half a day. Using this technique, the gravitational tides are completely removed from the SG
124 observational data, and now this remaining gravitational residual is subjected to the second step
125 of the SG data preprocessing, which was the correction for the pressure effect. The pressure
126 effect was corrected by multiplying the recorded barometric pressure variation P by a nominal

127 admittance of $-3 \text{ nm/s}^2/\text{hPa}$ [31]. After the pressure correction, we obtain the residual gravity
128 time series, which are shown in Fig 3 for the Japan and Chile earthquakes.



129

130 **Figure 3:** Gravity residuals during Japan and Chile earthquakes after the removal of gravity tides
131 and pressure corrections

132 We now perform a spectral analysis of this residual gravity time series. Fast Fourier transform
133 (FFT), wavelet analysis and maximum entropy spectrum are some of the methods reported in
134 previous studies that can be used for spectral analysis. The maximum entropy spectrum is
135 generally used for high frequency resolutions; however, it is only suitable for continuous signals.

136 Greater temporal resolution of observed signals is obtained with wavelet analysis, which is better
137 suited for signals such as transients or damped oscillations. The FFT is best suited to signals such
138 as harmonic signals because it has a high frequency resolution and can be used to detect free
139 oscillations of the earth. Here, we apply the FFT technique to search for EFO signals in gravity
140 residuals, and it is also effective in estimating signal-to-noise ratio of detected EFO modes. The
141 EFO consists of an infinite number of decaying sinusoids. This decreasing nature introduces
142 errors into the amplitude estimation by conventional Fourier analysis. To precisely identify the
143 EFO, the local amplitude estimate of each sinusoid in each segment was obtained, and the
144 attenuation in terms of quality factor Q was estimated from the amplitude variation of a
145 frequency given in successive windows. A multi-radix FFT routine was used to calculate the
146 Fourier transform, which does not require zero padding in the data. To further validate the
147 identification of EFO modes, the observed frequencies of the modes are compared to the
148 theoretical model based on different Earth models [21].

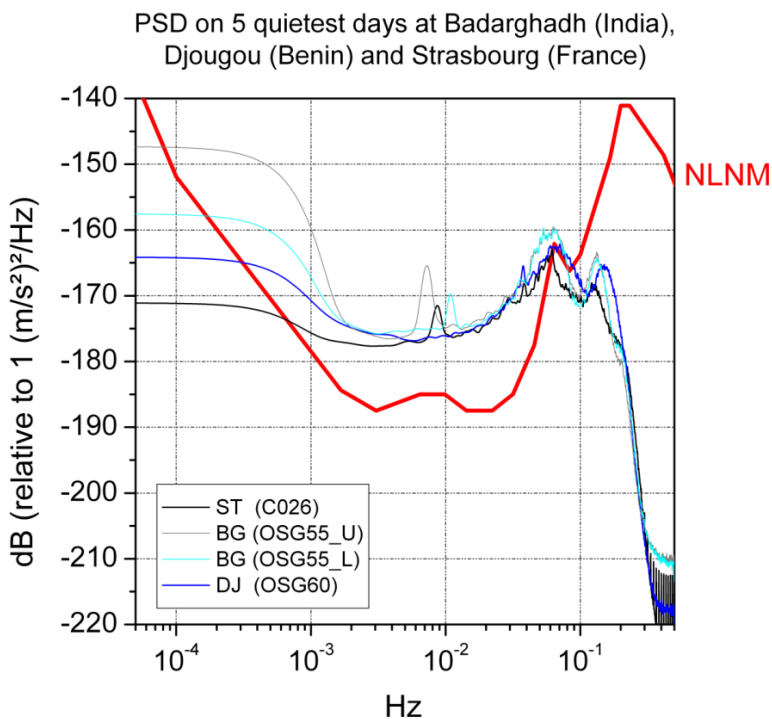
149

150 **2.1 Noise Characteristics of Badargadh station**

151 We are aware that SGs are renowned for their high sensitivity and low drift rates [8]. In order to
152 assess their ability to provide useful information for seismology, it is important to determine
153 their noise characteristics relative to other established instruments such as spring gravimeters and
154 other SG sites. As part of the International Geodynamics and Earth tides Service (IGETS),
155 around 18 superconducting gravimeters installed around the world have been connected. Since
156 all installed SG stations are networked, it is possible to compare the noise levels of different SG
157 stations. Understanding the noise levels at each location is essential for analyzing global earth
158 processes. Banka and Crossley [29] initiated the study of noise characteristics near SG sites.
159 Rosat et al. [32] developed a generalized method to study the noise characteristics at
160 seismological frequencies. Rosat and Hinderer [33] further standardized the method to check the
161 time stability of the noise characteristics of SG sites. To calculate noise characteristics at our SG
162 site in Badargadh Gujarat, we used the method initially proposed Banka and Crossley [29] and
163 generalized by Rosat and Hinderer [33].

164 We selected the five quietest days of the gravity time series based on their standard deviation
165 [29] to determine the noise characteristics at the Badargadh site. The combined instrument and

166 site noises in the long period range are revealed by the power spectral density (PSD) spectrum of
 167 the five quietest days [29, 32, 34]. We calculated the power spectral densities for both sensors
 168 because the Badargadh has a dual sensor SG and the results are shown in Fig 4. The PSDs are
 169 compared with the NLNM [35] which is used as a seismological noise reference. As expected,
 170 the PSD becomes lower than the NLNM at frequencies below 1 mHz where the SG data have
 171 been corrected for tides and atmospheric pressure effect. The site noise PSD spectrum of
 172 Badargadh SG is observed with PSDs ranging from -220 dB to -140 dB. This shows that the SG
 173 at the Badargadh site falls below a low noise site with a seismic noise magnitude (SNM) of 1.13.
 174 We also compared the noise level of the Badargadh site to some other SG sites around the world.
 175 Noise increases sharply at frequencies below 1 mHz. Such a characteristic is also observed in
 176 Djougou (DJ, Benin) and Strasbourg (ST, France).



177
 178 **Figure 4:** Comparison of SG near Badargadh with other SG sites from Djougou (DJ, Benin) and
 179 Strasbourg (ST, France). The new low noise model (NLNM) [35] is plotted as a reference.

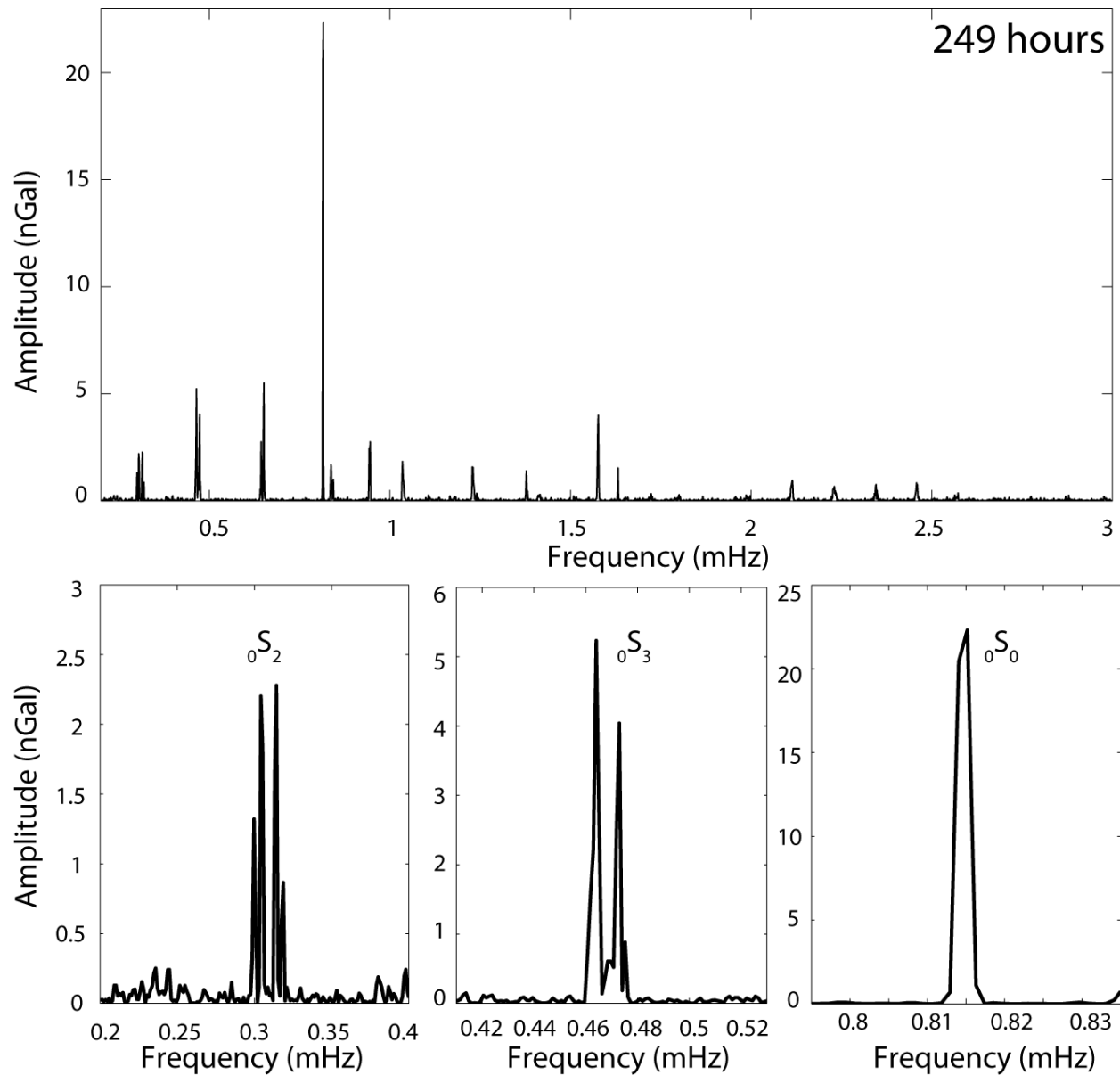
180 In fact, the higher noise level observed at frequencies below 1 mHz must be the result of using
 181 the wrong scale factor resulting in an adequate tidal model used for the reduction of data. Using
 182 theoretical solid tides for Gujarat, we estimated a scale factor of about $-814 \text{ nm/s}^2/\text{V}$ for Grav1
 183 and about $-775 \text{ nm/s}^2/\text{V}$ for Grav2. But it is a rough estimate as we used a solid earth tidal model
 184 whereas in Gujarat the ocean tides seem to be high. But using this estimated scale factor already

185 improves the low-frequency background noise. The spectral peak observed around 8-10 mHz for
186 the 4 SGs is due to the resonance mode of the levitating sphere which has a slightly different
187 period for each instrument.

188

189 **2.2 Identification of Free oscillations of the earth for 2011 Japan and 2010 Chile** 190 **earthquakes**

191 The residual gravity time series generated after the tidal and atmospheric corrections were
192 subjected to spectral analysis. If the instrument location has low ambient noise and we can use
193 barometric data to reduce the atmospheric pressure contribution, normal modes can be very
194 clearly identified using residual gravity data [36]. Since the ambient noise at the Badargadh site
195 is extremely low and the atmospheric pressure is reduced, we can identify normal modes here.
196 When the FFT is applied to the residual gravity time series after the Japan earthquake, which has
197 a duration of nearly 249 hours after the event and a frequency resolution ratio (FRR) of nearly
198 1.1155×10^{-6} /sec, it shows the spectrum in the low frequency band up to 20 mHz. Fig 5 shows
199 the spectrum up to 3 mHz, in which the gravest mode (${}_0S_2$), breathing mode (${}_0S_0$) and ${}_0S_3$ are
200 clearly visible. The splitting of ${}_0S_2$ and ${}_0S_3$ due to Earth's rotation and ellipticity is illustrated by
201 the presence of 4 and 3 spectral peaks respectively (Fig. 5). The Coriolis splitting is indeed
202 dominant for modes below 1 mHz [36]. Please note that because of the source-receiver
203 geometry, the singlet of ${}_0S_2$ corresponding to $m = 0$ is not visible at Gujarat station, while the 4
204 non-axial singlets are clearly visible. For ${}_0S_3$, only 3 singlets among the 7 are visible. Below 6
205 mHz, nearly 53 EFO modes were observed; of the 53 EFO modes, 47 represent the fundamental
206 spheroid modes. These observed EFO modes are fitted to a synthetic Lorentzian resonance
207 function to determine their frequency. We extract the error values for each mode as well as the
208 frequency using the method described by Dahlen et al. (1982) [37]. All the observed EFO modes
209 with their frequency and errors are listed in Table 1. We observed the frequency of 0.81468 mHz
210 for ${}_0S_0$ mode instead of the 0.81465 mHz in the PREM model. Similarly, the gravest mode ${}_0S_2$
211 mode is observed with 0.3100 mHz (i.e. 53.76 minutes) instead of the 0.3092 mHz (i.e. 54
212 minutes) in the PREM model the PREM model.

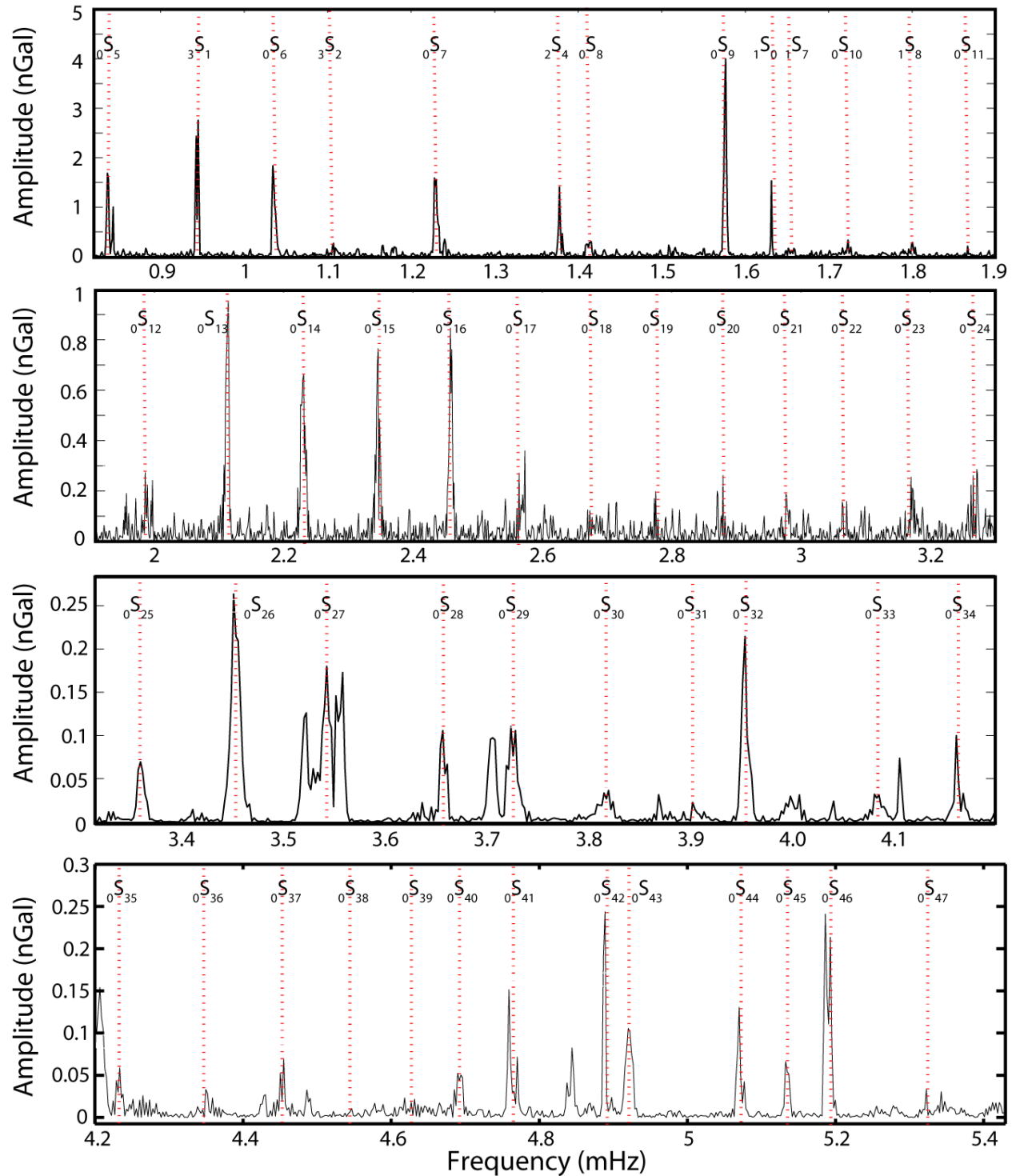


213

214

215

Figure 5: Spectrum of the Japan Earthquake after applying the FFT and the spectrum of the gravest mode (${}_0S_2$), breathing mode (${}_0S_0$) and the fundamental mode (${}_0S_3$).



216

217 **Figure 6:** Observed spheroidal modes from ${}_0S_4$ to ${}_0S_{48}$ after Japan Earthquake. Used data length:
 218 249 hours for modes ${}_0S_0$ to ${}_0S_{24}$ (top 2 panels); 120 hours for modes ${}_0S_{25}$ to ${}_0S_{47}$ (bottom 2 panels)

219 **Fig 6** shows the amplitude-frequency spectra of all other EFO modes identified after the Japan
 220 earthquake. All of the EFO modes that have been observed have frequency ranges between 0.1

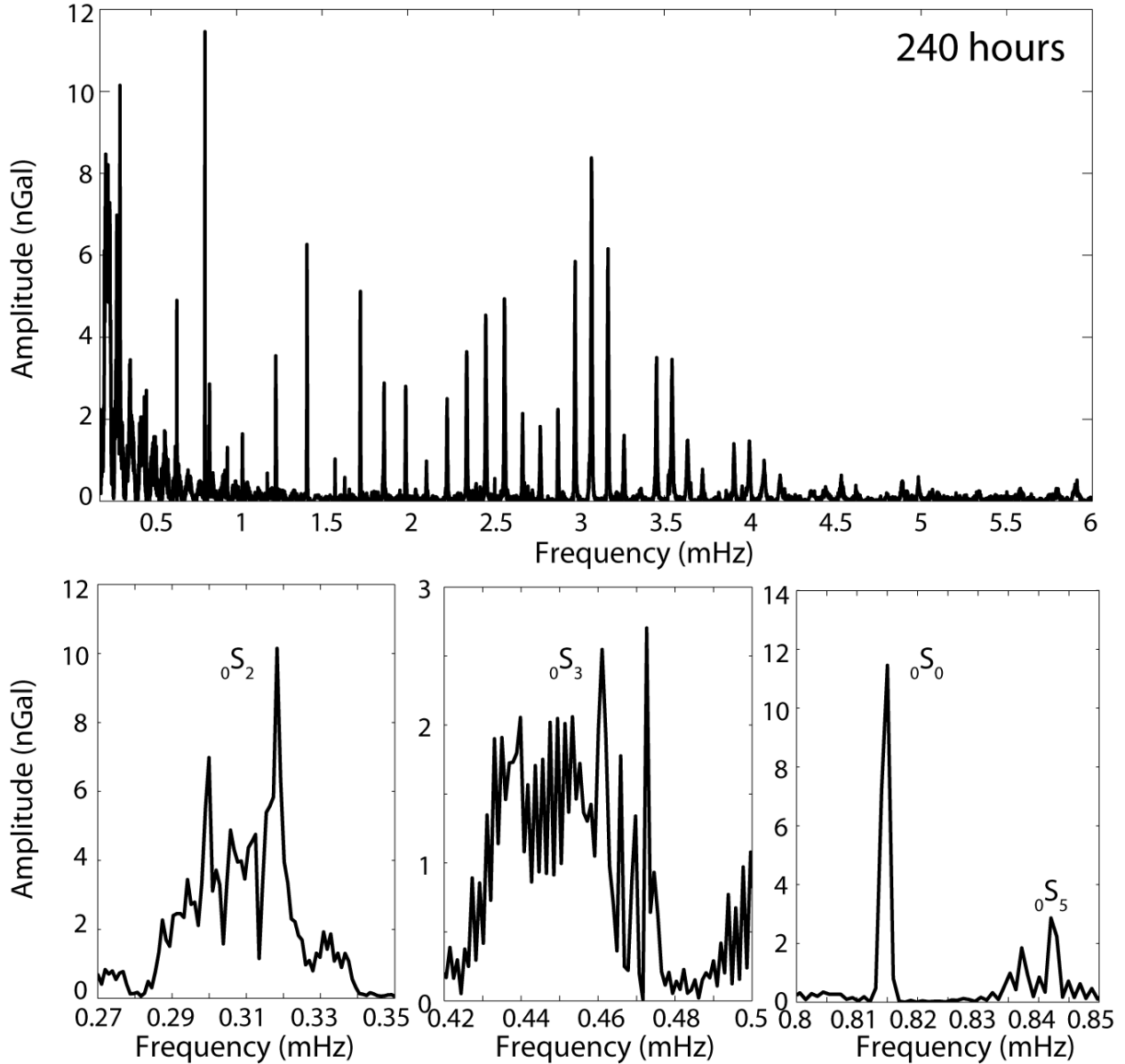
221 and 6 mHz. In addition to the 47 fundamental spheroidal modes, we were able to identify other
 222 EFO modes such as ${}_3S_1$, ${}_3S_2$, ${}_2S_4$, ${}_1S_0$, ${}_1S_7$ and ${}_1S_8$.

223 **Table 1:** Observed frequency and errors of EFO modes of Japan and Chile earthquakes

Mode	Observed Values (mHz)				Mode	Observed Values (mHz)			
	Japan		Chile			Japan		Chile	
	Frequency	Error	Frequency	Error		Frequency	Error	Frequency	Error
${}_0S_0$	0.81468	$\pm 5.7 \times 10^{-9}$	0.81469	$\pm 1.8 \times 10^{-8}$	${}_0S_{28}$	3.633	$\pm 1.7 \times 10^{-10}$	3.6367	$\pm 1.6 \times 10^{-10}$
${}_0S_2$	0.31006	$\pm 3.1 \times 10^{-5}$	0.30961	$\pm 1.1 \times 10^{-4}$	${}_0S_{29}$	3.7139	$\pm 7.5 \times 10^{-12}$	3.7317	$\pm 3.6 \times 10^{-11}$
${}_0S_3$	0.47072	$\pm 4.9 \times 10^{-4}$	0.46943	$\pm 2.5 \times 10^{-5}$	${}_0S_{30}$	3.8102	$\pm 1.2 \times 10^{-10}$	3.8184	$\pm 1.1 \times 10^{-7}$
${}_0S_4$	0.64949	$\pm 2.2 \times 10^{-4}$	0.65021	$\pm 4.1 \times 10^{-4}$	${}_0S_{31}$	3.9001	$\pm 7.6 \times 10^{-11}$	3.9127	$\pm 6.5 \times 10^{-11}$
${}_0S_5$	0.83951	$\pm 5.1 \times 10^{-13}$	0.83557	$\pm 7.1 \times 10^{-4}$	${}_0S_{32}$	3.993	$\pm 1.1 \times 10^{-10}$	3.9975	$\pm 4.9 \times 10^{-8}$
${}_0S_6$	1.0359	$\pm 5.2 \times 10^{-9}$	1.0362	$\pm 9.3 \times 10^{-6}$	${}_0S_{33}$	4.0854	$\pm 7.8 \times 10^{-11}$	4.0804	$\pm 4.5 \times 10^{-8}$
${}_0S_7$	1.2296	$\pm 3.2 \times 10^{-9}$	1.2295	$\pm 2.5 \times 10^{-9}$	${}_0S_{34}$	4.1784	$\pm 6.1 \times 10^{-11}$	4.1827	$\pm 2.9 \times 10^{-11}$
${}_0S_8$	1.4121	$\pm 1.2 \times 10^{-8}$	1.4117	$\pm 5.7 \times 10^{-9}$	${}_0S_{35}$	4.2645	$\pm 7.3 \times 10^{-11}$	4.2342	$\pm 9.1 \times 10^{-12}$
${}_0S_9$	1.576	$\pm 3.5 \times 10^{-9}$	1.5753	$\pm 1.4 \times 10^{-9}$	${}_0S_{36}$	4.3556	$\pm 4.1 \times 10^{-11}$	4.3538	$\pm 4.2 \times 10^{-11}$
${}_0S_{10}$	1.7231	$\pm 1.1 \times 10^{-9}$	1.7232	$\pm 9.1 \times 10^{-10}$	${}_0S_{37}$	4.4514	$\pm 2.1 \times 10^{-11}$	4.4448	$\pm 4.9 \times 10^{-4}$
${}_0S_{11}$	1.8562	$\pm 1.7 \times 10^{-4}$	1.8568	$\pm 6.6 \times 10^{-10}$	${}_0S_{38}$	4.5304	$\pm 4.1 \times 10^{-11}$	4.5338	$\pm 2.9 \times 10^{-7}$
${}_0S_{12}$	1.9872	$\pm 4.8 \times 10^{-5}$	1.9885	$\pm 2.4 \times 10^{-9}$	${}_0S_{39}$	4.6193	$\pm 4.2 \times 10^{-11}$	4.6212	$\pm 7.9 \times 10^{-10}$
${}_0S_{13}$	2.1127	$\pm 3.5 \times 10^{-9}$	2.1104	$\pm 4.5 \times 10^{-8}$	${}_0S_{40}$	4.7092	$\pm 4.4 \times 10^{-11}$	4.713	$\pm 1.8 \times 10^{-4}$
${}_0S_{14}$	2.2302	$\pm 3.7 \times 10^{-9}$	2.2303	$\pm 2.2 \times 10^{-9}$	${}_0S_{41}$	4.8002	$\pm 3.6 \times 10^{-11}$	4.8237	$\pm 6.2 \times 10^{-10}$
${}_0S_{15}$	2.3456	$\pm 2.7 \times 10^{-9}$	2.3451	$\pm 1.9 \times 10^{-9}$	${}_0S_{42}$	4.8795	$\pm 2.4 \times 10^{-11}$	4.8977	$\pm 1.1 \times 10^{-4}$
${}_0S_{16}$	2.4582	$\pm 1.5 \times 10^{-9}$	2.4568	$\pm 1.5 \times 10^{-9}$	${}_0S_{43}$	4.9712	$\pm 2.6 \times 10^{-11}$	4.9864	$\pm 1.8 \times 10^{-7}$
${}_0S_{17}$	2.5996	$\pm 3.1 \times 10^{-10}$	2.566	$\pm 9.1 \times 10^{-10}$	${}_0S_{44}$	5.0606	$\pm 1.6 \times 10^{-11}$	5.0268	$\pm 1.8 \times 10^{-4}$
${}_0S_{18}$	2.6658	$\pm 1.1 \times 10^{-10}$	2.6719	$\pm 9.6 \times 10^{-10}$	${}_0S_{45}$	5.1518	$\pm 1.7 \times 10^{-11}$	-	-
${}_0S_{19}$	2.7792	$\pm 6.6 \times 10^{-4}$	2.7753	$\pm 6.9 \times 10^{-10}$	${}_0S_{46}$	5.241	$\pm 1.7 \times 10^{-11}$	-	-
${}_0S_{20}$	2.8864	$\pm 1.4 \times 10^{-5}$	2.8786	$\pm 1.4 \times 10^{-10}$	${}_0S_{47}$	5.3306	$\pm 1.4 \times 10^{-11}$	5.3373	$\pm 5.1 \times 10^{-3}$
${}_0S_{21}$	2.98	$\pm 1.9 \times 10^{-5}$	2.9781	$\pm 3.1 \times 10^{-10}$	${}_3S_1$	0.94371	$\pm 1.3 \times 10^{-8}$	-	-
${}_0S_{22}$	3.0713	$\pm 2.8 \times 10^{-10}$	3.0739	$\pm 2.7 \times 10^{-10}$	${}_3S_2$	1.1068	$\pm 3.1 \times 10^{-10}$	-	-
${}_0S_{23}$	3.1689	$\pm 4.6 \times 10^{-10}$	3.1707	$\pm 1.5 \times 10^{-10}$	${}_2S_4$	1.3778	$\pm 7.6 \times 10^{-9}$	-	-
${}_0S_{24}$	3.2715	$\pm 2.2 \times 10^{-10}$	3.255	$\pm 6.6 \times 10^{-11}$	${}_1S_0$	1.6315	$\pm 4.4 \times 10^{-9}$	1.6223	$\pm 1.2 \times 10^{-4}$
${}_0S_{25}$	3.3512	$\pm 3.7 \times 10^{-11}$	3.364	$\pm 2.7 \times 10^{-10}$	${}_1S_7$	1.6565	$\pm 8.6 \times 10^{-9}$	-	-
${}_0S_{26}$	3.46	$\pm 1.3 \times 10^{-3}$	3.4537	$\pm 1.6 \times 10^{-10}$	${}_1S_8$	1.7987	$\pm 2.2 \times 10^{-8}$	-	-
${}_0S_{27}$	3.5481	$\pm 1.6 \times 10^{-10}$	3.5414	$\pm 1.8 \times 10^{-10}$	${}_2S_8$	-	-	2.048	$\pm 1.5 \times 10^{-3}$

224
 225 Yan et al. (2016) [38] also found the spectral peaks of spheroidal modes between the frequency
 226 range of 1–4 mHz for the 2011 Japan earthquake. Compared to the PREM model, Cheng-Yin
 227 Chu et al. (2021) [39] found that all stimulated modes contain antinodes and that ${}_0S_9$ – ${}_0S_{43}$
 228 spheroidal modes show prominent spectral peaks below 5 mHz. Above this frequency, however,
 229 it is difficult to observe EFO modes because the high frequency modes rapidly decay to the noise
 230 level due to the assumed long time, making them difficult to observe. We observed amplitude

231 ranges of 0 to 25 nGals for all modes for the Japan earthquake with a window length of 249
232 hours for modes ${}_0S_0$ to ${}_0S_{24}$ and 120 hours for the other modes. Similarly, we observed the
233 amplitude range of 0 to 12 nGals for the Chile earthquake with a window length of 240 hours for
234 the ${}_0S_0$ to ${}_0S_{24}$ modes and 120 hours for the other modes. We found that the amplitudes of the
235 observed EFO modes decrease with increasing frequency, or in other words, the amplitude
236 decreases with increasing time. Nishida and Kobayashi [40] also reported that above 5 mHz it is
237 difficult to identify mode peaks because the constructive interference traveling wave is distorted
238 due to heterogeneity and attenuation of the internal structure of the Earth. Kamal & Manisha et al.
239 [5] obtained an amplitude range up to 40 nGal with a window length of almost 24 hours for the
240 whole spectrum up to 5 mHz. For the identical 2011 Japan and 2010 Chile earthquakes,
241 Zabravova et al. [41](2012) found that the amplitudes of EFO modes change drastically for
242 different data lengths. In their study, the amplitude of the ${}_0S_0$ mode was determined to be 21.4
243 nGal for a data length of 250 hours and 18 nGal for a data length of 450 hours. This indicates
244 that as the amount of data increases, the amplitude of the modes decreases. The results of our
245 study with a data length of 240-249 hours are similar to those of Zabravova et al. [41] (2012)
246 with a data length of 250 hours. For the Japan earthquake, we measured the amplitudes of ${}_0S_0$ is
247 22.32 nGal, ${}_0S_2$ is 2.279 nGal, and ${}_0S_3$ is 4.641 nGals. Similarly, for Chile earthquake, the
248 amplitude value of ${}_0S_0$ is 11.45 nGal, ${}_0S_2$ is 10.15 nGal, and ${}_0S_3$ is 2.703 nGals. Rosat et al. [42]
249 (2005) reported the amplitude of 8.4 nGal for the Peru earthquake (8.4 Mw) and 40 nGal for the
250 Sumatra earthquake (9.3) with a data length of 240 hours. For the Japan earthquake after the ${}_0S_0$
251 mode, the ${}_0S_9$ mode has the second-highest amplitude value, which is 3.996 nGal. The
252 amplitudes of high frequency modes below ${}_0S_{10}$, have shown identical values and a diminishing
253 trend. Similarly in the case of Chile earthquake, the amplitudes of EFO modes up to ${}_0S_{35}$ are
254 higher than the high frequency EFO modes that come after ${}_0S_{35}$. In comparison, the amplitudes
255 of the EFO modes for the earthquake in Japan are higher than the amplitudes of the EFO modes
256 for the earthquake in Chile. This conclusion can be related to the magnitude of the earthquake
257 since the magnitude of the earthquake in Japan is greater than that of the earthquake in Chile.



259

260 **Figure 7:** Spectrum of the FFT, gravest mode and the breathing mode after Chile Earthquake

261 Similarly, the EFO mode identification procedure is applied to the data of 2010 earthquake in

262 Chile; we used the data length of almost 240 hours for this earthquake with a frequency

263 resolution ratio (FRR) of $1.157 * 10^{-6}$ /sec. Again, we clearly identify 47 EFO modes, of which

264 45 are fundamental spherical modes, including gravest mode ${}_0S_2$ and the breathing mode ${}_0S_0$. The

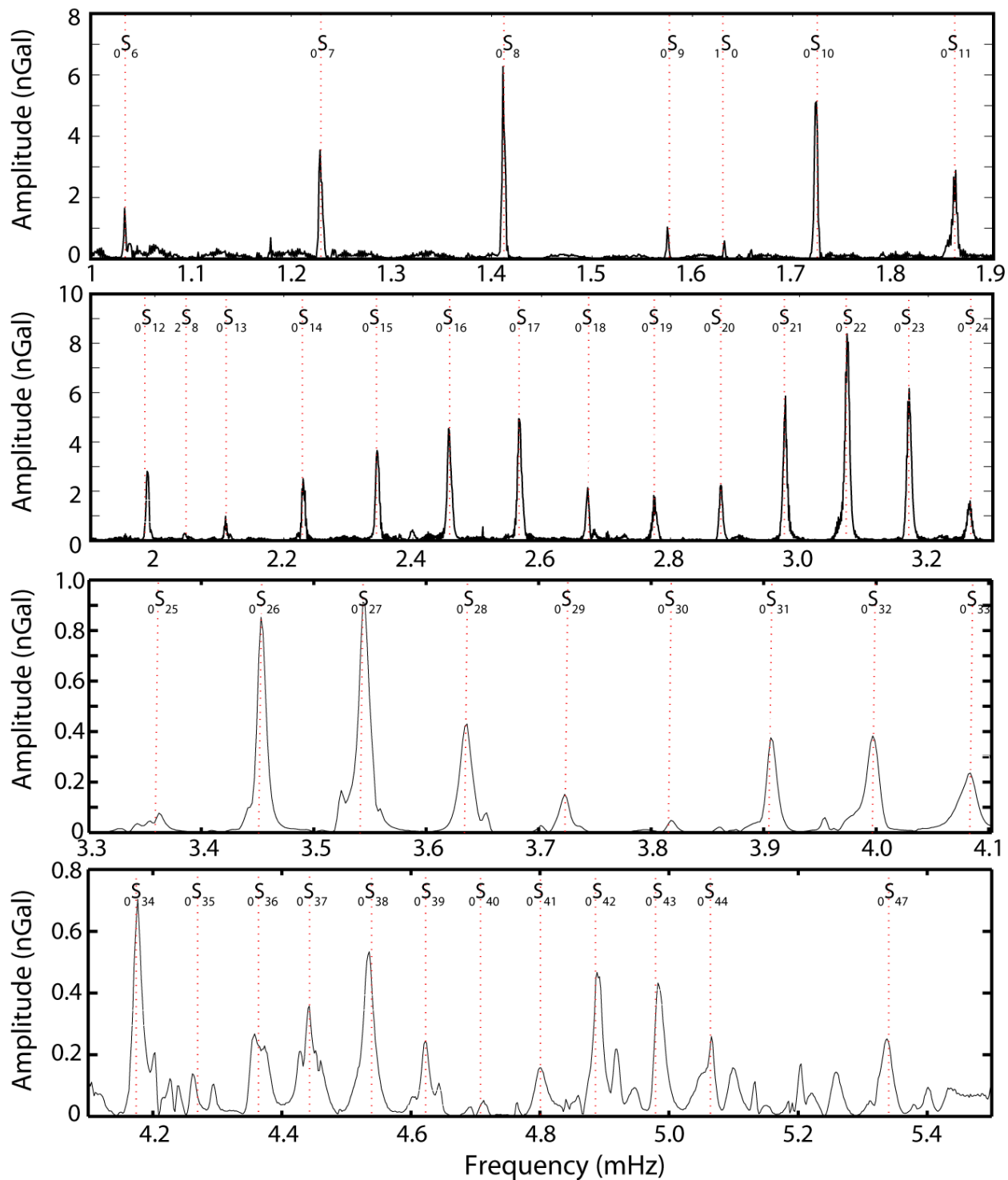
265 ${}_0S_0$ breathing mode was identified with a frequency of 0.81469 mHz for the Chile earthquake

266 instead of the frequency of 0.81465 mHz in the PREM model, and likewise the 45 observed

267 spheroidal nodes show reasonable agreement with the PREM model. The gravest mode ${}_0S_2$ mode

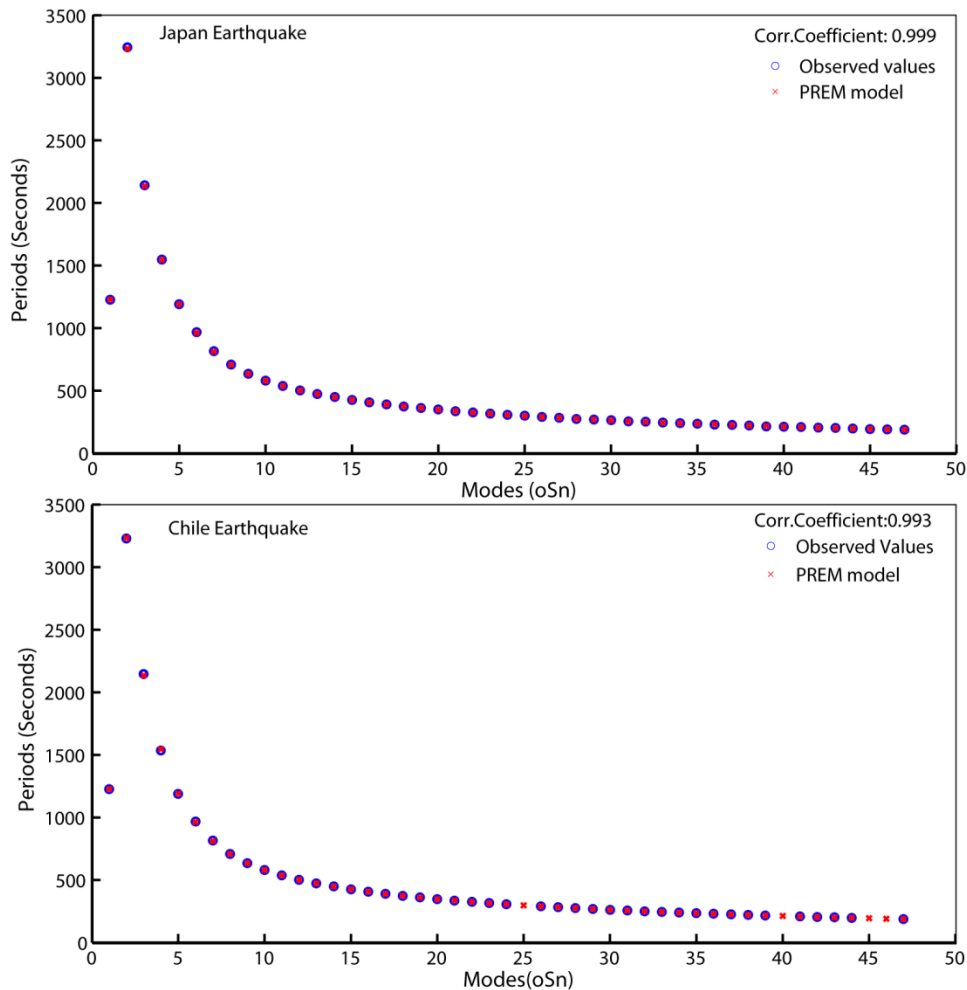
268 must be observed with 0.3092 mHz (i.e. 54 minutes) according to the PREM model, while it

269 occurs at 0.3096 mHz (i.e. 53.83 minutes) as in our observations for the Chile earthquake. The
 270 individual ${}_0S_3$ singlets (0.46855 mHz) and ${}_0S_2$ singlets due to the Coriolis effect is also visible.



271
 272 Figure 8: Observed spheroidal modes from ${}_0S_4$ to ${}_0S_{47}$ from Chile Earthquake. Used data length:
 273 240 hours for modes ${}_0S_0$ to ${}_0S_{24}$ (top 2 panels); 120 hours for modes ${}_0S_{25}$ to ${}_0S_{47}$ (bottom 2 panels)

274 Fig. 7 shows the FFT amplitude spectrum of the Chile earthquake, along with its gravest modes
 275 ${}_0S_2$, ${}_0S_3$ and breathing mode ${}_0S_0$. Fig. 8 shows the amplitude-frequency spectra for all other EFO
 276 modes identified after the Chile earthquake. The observed EFO modes ranging from ${}_0S_6$ to ${}_0S_{47}$
 277 are clearly visible in this figure, two of them ${}_0S_{45}$ and ${}_0S_{46}$ could not be identified. EFO modes
 278 such as ${}_1S_0$ and ${}_2S_8$ between these frequency ranges have also been identified. For this
 279 earthquake, we could only detect 47 fundamental modes below 6 mHz and could not locate clear
 280 spectral peaks above 6 mHz, while Wu Ye et al. (2013) [43] discovered about 76 different basic
 281 modes. We can also observe the amplitude ranges of these observed EFO modes, ranging from 0
 282 to 12 nGal for all the EFO modes in frequency ranges from 0.1 to 6 mHz. Beyond this frequency,
 283 it becomes difficult to observe the EFO modes because the noise masks the modes as observed in
 284 the case of the earthquake in Japan.



285
 286 **Figure 9:** Correlation between the Japan Observed EFO periods (left panel); the Chile Observed
 287 EFO periods (right panel) and the theoretical PREM model periods

288 Arora et al. [23] first reported the observation of EFO using data from a superconducting
289 gravimeter at Ghuttu, Uttarakhand in India. Later, Institute of Seismological Research installed
290 the second superconducting gravimeter in Badargadh, Gujarat, India. We are the second to report
291 the observation of EFO in India. Our observatory is located in western India while their
292 observatory is located in northern India. Arora et al. [23] used data from the 2008 Solomon
293 Islands earthquake (M 8.1) and reported almost 42 spheroidal modes. We were able to identify
294 47 EFO modes from the 2010 earthquake in Chile and 53 EFO modes from the 2011 earthquake
295 in Japan. We obtained a correlation coefficient of 0.999 for Japan earthquake and 0.993 for Chile
296 earthquake by comparing the observed frequencies with those predicted by the theoretical PREM
297 model, indicating a strong correlation between the observed observations and the PREM
298 observations. Fig. 9 illustrates the correlation between the periods observed in Japan; the periods
299 observed in Chile and the periods of the PREM model. By comparing the amplitudes of the
300 modes, we find that the amplitude of the ${}_0S_0$ mode of the Japan earthquake is 22.32 nGal, while
301 the amplitude of the Chile earthquake is 11.46 nGal for the same ${}_0S_0$ mode. These EFO modes
302 have different amplitudes but their frequencies are the same. If we look at the amplitudes of all
303 EFO modes for earthquakes in Japan, the ${}_0S_9$ mode comes second with a measurement of 3.996
304 nGal. The amplitude values of all the other detected EFO modes are then almost identical for
305 both the earthquakes. Until mode ${}_0S_{35}$, we find that the amplitudes of the EFO modes of the
306 earthquake in Chile are comparable, but for higher-frequency modes, we find a decrease in their
307 amplitudes. The measured EFO mode amplitudes of Japan earthquake are larger compared to the
308 EFO mode amplitudes for the Chile earthquake. The amplitudes of these two earthquakes also
309 showed a correlation, giving a correlation factor of 0.47%. It is possible to detect earthquakes at
310 low frequencies without knowing them at high frequencies by comparing the spectral levels in
311 small bands centered on the known frequencies of typical resonance peaks to the spectral levels
312 of the background noise [44]. Thus, the unambiguous identification of normal low-frequency
313 modes undoubtedly opens up new possibilities for studying low-frequency seismological
314 research where conventional seismometers fail.

315

316

317

318 **2.3 Comparison of the observed periods of EFO modes with the previous observations.**

319 We applied the Fast Fourier Transform (FFT) technique to the Hanning-windowed residual
 320 gravity time series to obtain the frequency-amplitude spectra. Using the Lorentzian fitting, we
 321 obtain the frequency and error of all observed EFO modes. These frequency values are converted
 322 into periods. To identify EFO modes, these peak frequency values are compared to the
 323 theoretical frequencies of the EFO modes for the PREM model. In this section, we compare
 324 observed EFO mode periods to previously published observational and theoretical values. For
 325 this, we used results published in the study by Ness et al. [21]; Derr [45] and Dziewonski &
 326 Gilbert [46]. We have taken the theoretical periods of the spheroidal modes of Haddon and
 327 Bullen [47]; and Jordan and Anderson [48]. Table 2 contains a list of all the periods of observed
 328 EFO and other studies. We first calculated the relative variance of our observed periods with
 329 previously published observations and theoretical values to validate the results of our study. It
 330 uses the ratio of the difference between the theoretical and observed values to the observed
 331 values to calculate the relative deviation (RD). Fig. 10 shows the relative deviation of these
 332 observation periods after Japan and Chile earthquakes compared to the periods of the PREM
 333 model and to previous observations.

334 **Table 2:** Periods of observed EFO modes; previous results and theoretical values

Mode	Observed Periods (seconds)		PREM (S)	Ob_1 (s)	Ob_2 (s)	Ob_3 (s)	Th_1 (s)	Th_2 (s)
	Japan	Chile						
${}_0S_0$	1227.48	1227.46	1227.52	1227.7	1227.64	1227.64	1228.8	1227.61
${}_0S_2$	3225.18	3229.87	3234.15	3233.1	3233.3	3233.3	3226.9	3232.45
${}_0S_3$	2124.41	2130.24	2134.93	2139.2	2133.56	2133.56	2135.6	2134.13
${}_0S_4$	1539.67	1537.96	1545.83	1546	1547.16	1547.3	1547.2	1545.82
${}_0S_5$	1191.17	1196.79	1190.19	1188.4	1189.3	1190.12	1191.4	1190.42
${}_0S_6$	965.34	965.06	963.21	962.3	963.94	963.17	964.3	963.72
${}_0S_7$	813.27	813.34	811.49	809.1	811.67	811.45	812.5	812.24
${}_0S_8$	708.17	708.37	707.66	707.7	707.57	707.64	707.9	707.7
${}_0S_9$	634.52	634.80	633.91	634	634.01	633.95	633.9	633.69
${}_0S_{10}$	580.35	580.32	579.37	579.3	580.04	580.08	579.4	579.19
${}_0S_{11}$	538.74	538.56	536.91	536.8	536.46	536.56	537.1	536.87
${}_0S_{12}$	503.22	502.89	502.36	502.3	502.03	502.18	502.6	502.34
${}_0S_{13}$	473.33	473.84	473.17	473.2	473.05	473.14	473.5	473.21
${}_0S_{14}$	448.39	448.37	448.21	448.4	448.37	448.28	448.4	448.1
${}_0S_{15}$	426.33	426.42	426.17	426.3	426.19	426.24	426.4	426.16
${}_0S_{16}$	406.80	407.03	406.77	406.8	406.54	406.77	407	406.79
${}_0S_{17}$	384.67	389.71	389.41	389.3	389.37	389.31	389.7	389.56

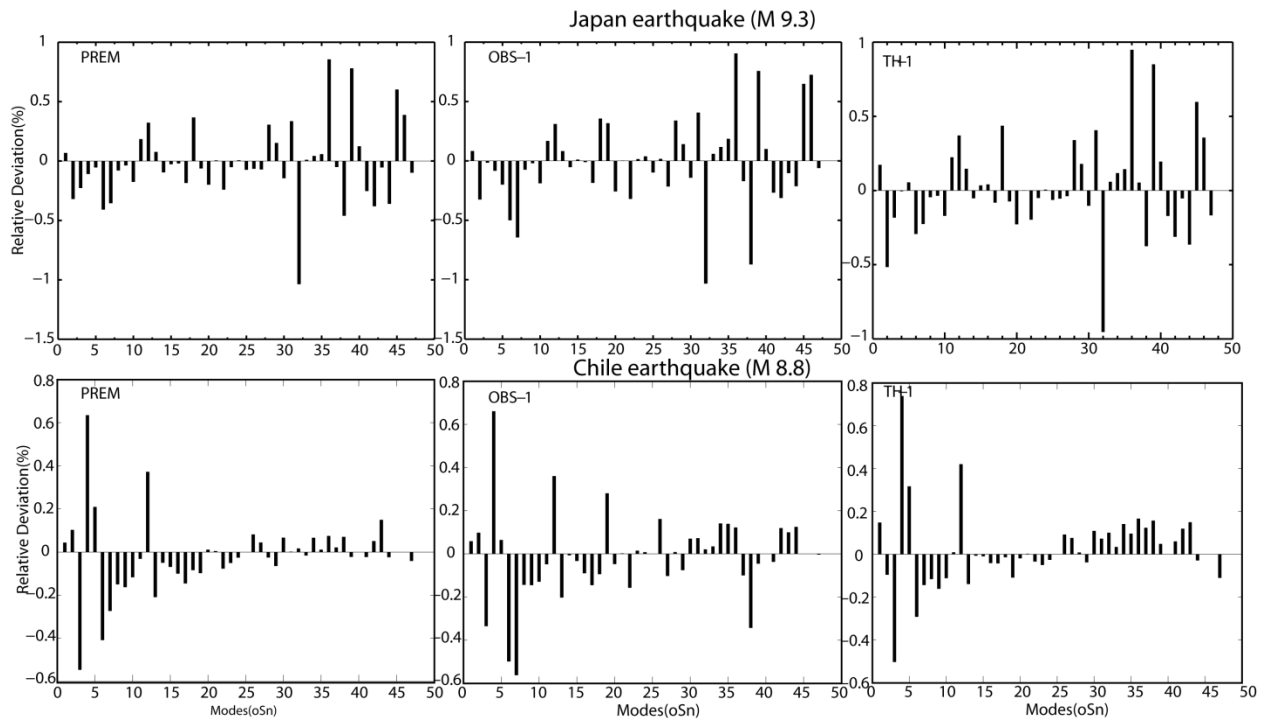
${}_0S_{18}$	375.12	374.27	373.94	373.9	373.39	373.89	374.2	374.1
${}_0S_{19}$	359.82	360.32	360.15	361.5	360.57	360.2	360.1	360.14
${}_0S_{20}$	346.45	347.39	347.51	347.3	347.39	347.82	347.4	347.47
${}_0S_{21}$	335.57	335.78	335.82	335.8	335.8	336	335.8	335.88
${}_0S_{22}$	325.60	325.32	325.07	324.8	325.07	325.31	325.2	325.23
${}_0S_{23}$	315.57	315.39	315.31	315.5	315.11	315.43	315.3	315.38
${}_0S_{24}$	305.67	307.22	306.20	306.3	306.1	306.25	306.2	306.24
${}_0S_{25}$	298.40	297.26	297.67	297.6	297.54	297.71	297.7	297.72
${}_0S_{26}$	289.02	289.54	289.69	289.9	289.48	289.69	289.7	289.74
${}_0S_{27}$	281.84	282.37	282.21	281.8	282.38	282.34	282.3	282.25
${}_0S_{28}$	275.25	274.97	275.18	275.2	274.87	275.06	275.2	275.18
${}_0S_{29}$	269.26	267.97	268.46	268.4	268.27	268.44	268.5	268.49
${}_0S_{30}$	262.45	261.89	262.10	262.1	261.94	262.15	262.2	262.15
${}_0S_{31}$	256.40	255.58	256.02	256.2	256.02	256	256.2	256.12
${}_0S_{32}$	250.44	250.16	250.31	250.3	250.09	250.2	250.5	250.38
${}_0S_{33}$	244.77	245.07	244.88	245	245.3	244.95	245	244.91
${}_0S_{34}$	239.33	239.08	239.62	239.8	239.87	239.7	239.8	239.67
${}_0S_{35}$	234.49	236.17	234.60	234.9	234.51	234.69	234.8	234.66
${}_0S_{36}$	229.59	229.68	229.80	229.9	229.66	229.74	230	229.85
${}_0S_{37}$	224.65	224.98	225.17	224.9	224.75	225.16	225.4	225.24
${}_0S_{38}$	220.73	220.57	220.71	219.8	220.08	220.62	220.9	220.8
${}_0S_{39}$	216.48	216.39	216.45	216.4	216.45	216.43	216.6	216.54
${}_0S_{40}$	212.35	212.18	212.35	212.3	212.09	212.31	212.5	212.43
${}_0S_{41}$	208.32	207.31	208.33	208.3	207.88	208.05	208.5	208.47
${}_0S_{42}$	204.94	204.18	204.56	204.7	204.54	204.57	204.7	204.65
${}_0S_{43}$	201.16	200.55	200.90	200.8	201	200.93	200.9	200.96
${}_0S_{44}$	197.61	198.93	197.31	197.6	197.51	197.19	197.3	197.4
${}_0S_{45}$	194.11	-	193.91	194	193.91	194.03	193.9	193.95
${}_0S_{46}$	190.80	-	190.56	191.2	190.89	190.59	190.5	190.62
${}_0S_{47}$	187.60	187.36	187.33	187.4	187.48	187.43	187.2	187.4
${}_3S_1$	1059.65	-	1058.09	-	-	-	-	-
${}_3S_2$	903.51	-	904.32	-	-	-	-	-
${}_2S_4$	725.79	-	724.85	-	-	-	-	-
${}_1S_0$	612.93	616.41	613.01	-	-	-	-	-
${}_1S_7$	603.68	-	604.23	-	-	-	-	-
${}_1S_8$	555.95	-	556.02	-	-	-	-	-
${}_2S_8$	-	488.28	488.19	-	-	-	-	-

335 Obs_1=Ness et al. [21] Values, Obs_2= Derr [45] values, Obs_3= Dziewonski & Gilbert [46]
336 values, Th_1= HB1 model [47], Th_2= Jordan and Anderson model [48].

337

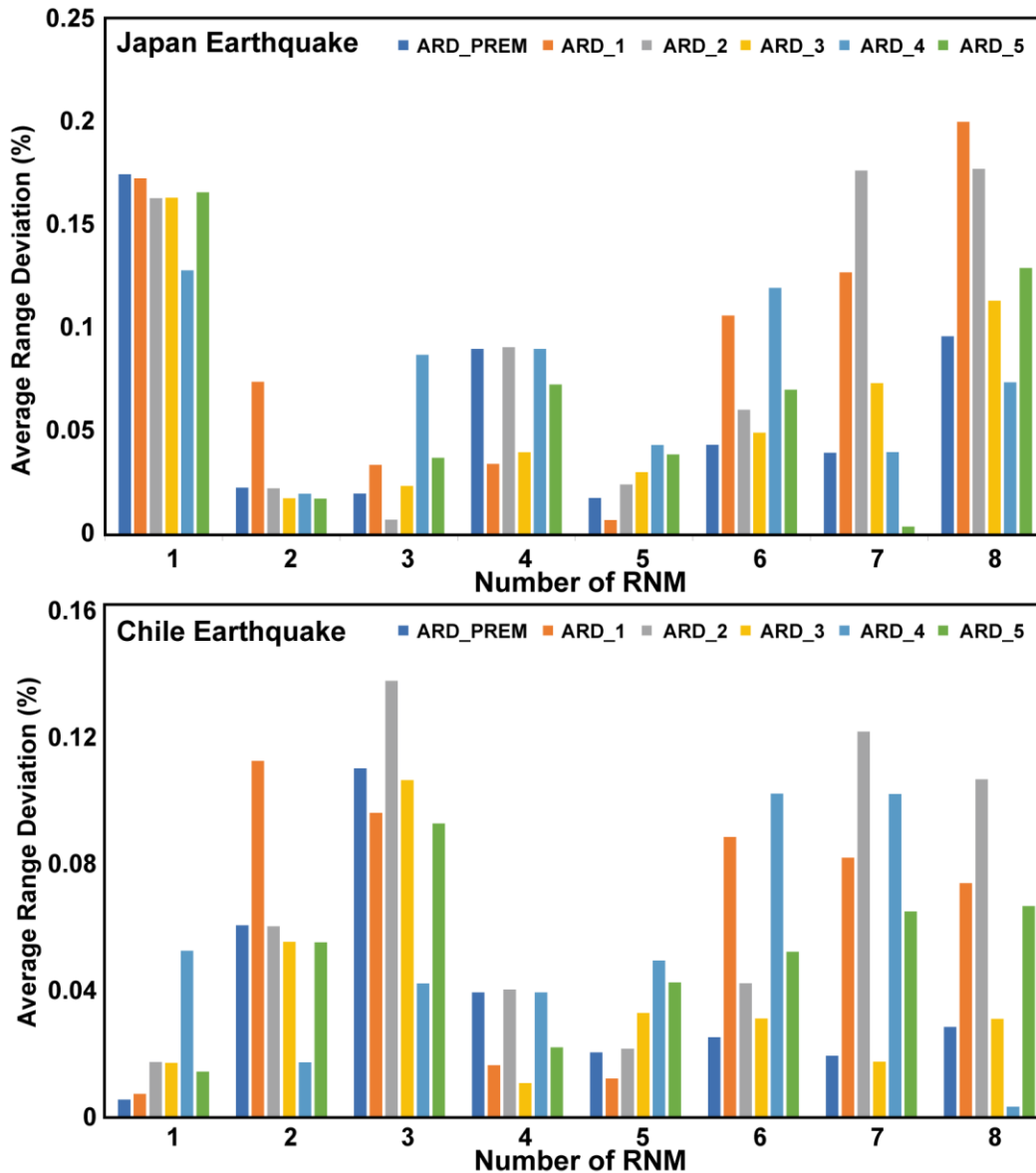
338 We determined the relative deviation values of our observed spheroidal modes with the PREM
339 model [13], Ness et al. [21](Obs_1), model HB1 [47](Th_1), we find that most modes have a
340 relative deviation value less than or equal to 0.5%, with a few exceptions, some modes such as

341 ${}_0S_{32}$, ${}_0S_{36}$ and ${}_0S_{39}$ in the case of Japan earthquake. Most of the modes from ${}_0S_0$ to ${}_0S_{30}$ show more
 342 relative deviations, which can reach up to 0.1% compared to the other modes. In the case of the
 343 Chile earthquake, the modes ${}_0S_3$ & ${}_0S_4$ with the values of the PREM model [13] and the HB1
 344 model [47] (Th_1), as well as ${}_0S_4$, ${}_0S_6$ & ${}_0S_7$ with Ness et al. [21] (Obs_1), the values show
 345 relative deviations of more than 0.5%.



346
 347 **Figure 10:** Relative Deviations of the observed periods with PREM model, Ness et al. [20]
 348 observations and the HB1 model [47]

349
 350 Modes from ${}_0S_0$ to ${}_0S_{30}$ show a larger relative deviation from previous observations compared to
 351 modes from ${}_0S_{31}$ to ${}_0S_{43}$. We then subdivide the 47 spheroidal modes into 8 groups, each group
 352 containing 6 spheroidal modes, to further validate our observed results. Additionally, we
 353 calculate the mean relative deviation (ARD) for that specific range of normal modes, which is
 354 the average of the relative deviation values for each normal mode in a single RNM [47]. There
 355 are six different types of spheroid mode periods that we can use to calculate the relative
 356 deviation from our observed spheroidal mode periods. Therefore, there are six average relative
 357 deviations (ARD) for each normal mode range. Fig. 11 shows the ARDs for all RNMs for the
 358 Chile and Japan earthquakes.



359

360 **Figure 11:** Average Relative Deviation of all the Range of Normal modes. ARD_1:Average
 361 Relative Deviation with Ness et al.,[21] observations, ARD_1: Average Relative Deviation with
 362 Deer [45] observations. ARD_3: Average Relative Deviation with Dziewonski &Gilbert [46]
 363 observations. ARD_4: Average Relative Deviation with HB1 model [47] observations, ARD_5:
 364 Average Relative Deviation with Jordan &Anderson model [48] observations and ARD_PREM:
 365 Average Relative Deviation with PREM model observations [13]

366

367 In connection with the observations of the Japan earthquake, we note that all of the 8 RNMs,
 368 except the first, have an average relative deviation (ARD) of 0.1%. The first RNM, on the other
 369 hand, has an ARD value of 0.18%. For RNMs 4 and 5, we noticed that only observations with
 370 Ness et al. [21] (ARD_1) & Derr [45](ARD_2) show a larger average relative deviation, which

371 has a value greater than 0.1%. As with the Chile earthquake, all RNMs except RNM 3 have ARD
372 values less than or equal to 0.1%. In RNM 3, all observations have higher ARD values than other
373 RNMs. We also note that in RNMs 3, 7 and 8, observations with Derr [45] (ARD_2) have ARD
374 values greater than 0.1%. These results from the two earthquakes show that modes from ${}_0S_0$ to
375 ${}_0S_{30}$ deviate more than the modes from ${}_0S_{31}$ to ${}_0S_{47}$. Lei et al. [49] reported that a larger relative
376 deviation is found for ${}_0S_2$, ${}_0S_3$ spheroidal modes with the theoretical periods of these modes.
377 Similarly, we find that modes from ${}_0S_0$ to ${}_0S_{30}$ exhibit larger relative deviations from previous
378 observations and theoretical values.

379

380 **3. Conclusions**

381 In this paper, observations of free oscillations of the Earth are presented, obtained during two
382 major earthquakes, the Japan and Chile earthquakes that occurred in 2011 and 2010,
383 respectively. Based on comparisons of the noise characteristics of the Badargadh site with some
384 other SG sites around the world, our SG site is classified as a low seismic noise site with a
385 seismic noise magnitude (SNM) of 1.13 such as defined in Banka and Crossley (1999) [28]. We
386 find that the noise increases at frequencies below 1 mHz. Such a characteristic is also observed
387 in SG stations of Djougou (Benin, Africa) and Strasbourg (France). The scale factor for the two
388 spheres of SG is calculated using theoretical solid tides and is $-814 \text{ nm/s}^2/\text{V}$ for Grav1 (lower
389 sphere) and $-775 \text{ nm/s}^2/\text{V}$ for Grav2 (upper sphere). We were able to detect 53 EFO modes from
390 the Japan earthquake and 47 EFO modes from the Chile earthquake using spectrum analysis,
391 including breathing modes and gravest modes below 1 mHz. The frequencies of all these
392 observed modes were correlated with predictions from the PREM model, giving a correlation
393 factor of 0.999 for the Japan earthquake and 0.993 for the Chile earthquake, indicating that the
394 resulting EFO modes are accurate. This validates the quality of the data useful for low frequency
395 studies in seismology. The relative deviations of our observed EFO modes from previous
396 observations show that the relative deviation does not exceed 0.5%, which means that our results
397 correlate satisfactorily with previous studies.

398 **Acknowledgement**

399 The authors thank the Director General of the Institute of Seismological Research (ISR),
400 Gandhinagar, for permission to carry out the work. The authors express their sincere gratitude to

401 the Department of Science and Technology, Government of Gujarat for providing the necessary
402 funds for the study. The authors thank the organizers of the 19th International Symposium on
403 Geodynamics and Earth Tides (G-ET 2021) on June 22-23, 2021. The authors thank two
404 anonymous reviewers and Dr. Yiyang Zhou, Editor-in-Chief, Geodesy and Geodynamics, for their
405 constructive comments which greatly improved the manuscript.

406 **4. References**

- 407 1 Buland, Ray. "Free oscillations of the Earth." *Annual Review of Earth and Planetary Sciences* 9
408 (1981): 385-413.
- 409 2 Dahlen, FAand, and Jeroen Tromp. "Theoretical global seismology." *Theoretical Global Seismology*.
410 Princeton university press, (1998).
- 411 3 Masters, Guy, and Freeman Gilbert. "Structure of the inner core inferred from observations of its
412 spheroidal shear modes." *Geophysical Research Letters* 8.6 (1981): 569-571.
- 413 4 Zürn, W., A.M.G. Ferreira, R. Widmer-Schmidrig, K. Lentas, L. Rivera, E. Clévéde, High-quality
414 lowest-frequency normal mode strain observations at the Black Forest Observatory (SW-Germany)
415 and comparison with horizontal broad-band seismometer data and synthetics, *Geophysical Journal*
416 *International*, Volume 203, Issue 3, December (2015), Pages 1787–1803,
417 <https://doi.org/10.1093/gji/ggv381>
- 418 5 Kamal and Mansinha, L.; A test of the superconducting gravimeter as a long-period seismometer,
419 *Phys. Earth Planet. Int.* (1992) 71, 52–60.
- 420 6 Zürn, W., and H-G. Wenzel. "High quality data from La Coste-Romberg gravimeters with
421 electrostatic feedback: A challenge for superconducting gravimeters." *Marées terrestres*
422 *(Bruxelles)* 110 (1991): 7940-7952.
- 423 7 Crossley, D., et al. "Network of superconducting gravimeters benefits a number of disciplines." *Eos*,
424 *Transactions American Geophysical Union* 80.11 (1999): 121-126. 10.1029/99EO00079
- 425 8 Van Camp, M. "Measuring seismic normal modes with the GWR C021 superconducting
426 gravimeter." *Physics of the Earth and Planetary Interiors* 116.1-4 (1999): 81-92.
- 427 9 Zürn, W., and R. Widmer. "On noise reduction in vertical seismic records below 2 mHz using local
428 barometric pressure." *Geophysical Research Letters* 22.24 (1995): 3537-3540.
- 429 10 Benioff, Hugo, Frank Press, and Stewart Smith. "Excitation of the free oscillations of the Earth by
430 earthquakes." *Journal of Geophysical Research* 66.2 (1961): 605-619.
- 431 11 Tanimoto, Toshiro. "Continuous free oscillations: atmosphere-solid earth coupling." *Annual Review*
432 *of Earth and Planetary Sciences* 29.1 (2001): 563-584.
- 433 12 Nishida, Kiwamu. "Earth's background free oscillations." *Annual Review of Earth and Planetary*
434 *Sciences* 41 (2013): 719-740.
- 435 13 Dziewonski, Adam M., and Don L. Anderson. "Preliminary reference Earth model." *Physics of the*
436 *earth and planetary interiors* 25.4 (1981): 297-356.
- 437 14 Smith, Stewart Wilson. *An investigation of the earth's free oscillations*. Diss. California Institute of
438 Technology, (1961).
- 439 15 Lowrie, William, and Andreas Fichtner. *Fundamentals of geophysics*. Cambridge university press,
440 2020.
- 441 16 He, Xiong, and Jeroen Tromp. "Normal- mode constraints on the structure of the Earth." *Journal of*
442 *Geophysical Research: Solid Earth* 101.B9 (1996): 20053-20082.

- 443 17 Giardini, Domenico, Xiang- Dong Li, and John H. Woodhouse. "Splitting functions of long- period
444 normal modes of the Earth." *Journal of Geophysical Research: Solid Earth* 93.B11 (1988): 13716-
445 13742.
- 446 18 Park, Jeffrey, et al. "Earth's free oscillations excited by the 26 December 2004 Sumatra-Andaman
447 earthquake." *Science* 308.5725 (2005): 1139-1144.
- 448 19 Jiang, Ying, et al. "Constraining the focal mechanism of the Lushan earthquake with observations of
449 the Earth's free oscillations." *Science China Earth Sciences* 57.9 (2014): 2064-2070.
- 450 20 Zábránová, E., et al. "Constraints on the centroid moment tensors of the 2010 Maule and 2011
451 Tohoku earthquakes from radial modes." *Geophysical research letters* 39.18 (2012).
- 452 21 Ness, N. F., J. C. Harrison, and L. B. Slichter. "Observations of the free oscillations of the
453 earth." *Journal of Geophysical Research* 66.2 (1961): 621-629.
- 454 22 Imanishi, Yuichi, et al. "A network of superconducting gravimeters detects submicrogal coseismic
455 gravity changes." *Science* 306.5695 (2004): 476-478.
- 456 23 Arora, B. R., et al. "First observations of free oscillations of the earth from Indian superconducting
457 gravimeter in Himalaya." *Current Science* (2008): 1611-1617.
- 458 24 Richter, B., et al. "From Chandler wobble to free oscillations: comparison of cryogenic gravimeters
459 and other instruments in a wide period range." *Physics of the Earth and Planetary Interiors* 91.1-3
460 (1995): 131-148.
- 461 25 Prothero Jr, W. A., and J. M. Goodkind. "A superconducting gravimeter." *Review of Scientific
462 Instruments* 39.9 (1968): 1257-1262.
- 463 26 Goodkind, John M. "The superconducting gravimeter." *Review of scientific instruments* 70.11 (1999):
464 4131-4152.
- 465 27 Harnisch, M., et al. The dual sphere superconducting gravimeter GWR. Geodesy Beyond 2000: The
466 Challenges of the First Decade, IAG General Assembly Birmingham, July 19–30, 1999 *121* (2000):
467 155
- 468 28 Van Camp, M., and Vauterin, P., "Tsoft: graphical and interactive software for the analysis of time
469 series and Earth tides" *Computers & Geosciences*, 31(5), (2005) 631-640, doi:
470 10.1016/j.cageo.2004.11.015,.
- 471 29 Banka, Dirk, and David Crossley. "Noise levels of superconducting gravimeters at seismic
472 frequencies." *Geophysical Journal International* 139.1 (1999): 87-97.
- 473 30 Dehant, V., Defraigne, P., Wahr, J., Tides for a convective earth. *J. Geophys. Res.* 104 (B1), (1999)
474 1035–1058.
- 475 31 Merriam, J.B., Atmospheric pressure and gravity. *Geophys. J. Int.* 109 (3), (1992) 488–500.
- 476 32 Rosat, S., J. Hinderer, D. Crossley, and J. P. Boy, Performance of superconducting gravimeters from
477 long-period seismology to tides, *J. Geodyn.*, 38(3 - 5), (2004) 461– 476..
- 478 33 Rosat, Séverine, and Jacques Hinderer. "Noise levels of superconducting gravimeters: updated
479 comparison and time stability." *Bulletin of the Seismological Society of America* 101.3 (2011): 1233-
480 1241.
- 481 34 Riccardi, U., Séverine Rosat, and Jacques Hinderer. "Comparison of the Micro-g LaCoste gPhone-
482 054 spring gravimeter and the GWR-C026 superconducting gravimeter in Strasbourg (France) using a
483 300-day time series." *Metrologia* 48.1 (2011): 28.
- 484 35 Peterson, Jon R. *Observations and modeling of seismic background noise*. No. 93-322. US Geological
485 Survey, (1993).
- 486 36 Widmer-Schmidrig, R. "What can superconducting gravimeters contribute to normal-mode
487 seismology?." *Bulletin of the Seismological society of America* 93.3 (2003): 1370-1380.
- 488 37 Dahlen, F. A. "The effect of data windows on the estimation of free oscillation
489 parameters." *Geophysical Journal International* 69.2 (1982): 537-549.

- 490 38 Yan, Rui, et al. "Earth's free oscillations excited by the 2011 Tohoku M w 9.0 earthquake detected
491 with a groundwater level array in mainland China." *Geophysical Journal International* 206.3 (2016):
492 1457-1466.
- 493 39 Cheng-Yin, Chu, et al. "Earth's free oscillations excited by the 2011 Tohoku earthquake recorded in
494 multiple GPS networks." *Earth, Planets and Space (Online)* 73.1 (2021).
- 495 40 Nishida, Kiwamu, and Naoki Kobayashi. "Statistical features of Earth's continuous free
496 oscillations." *Journal of Geophysical Research: Solid Earth* 104.B12 (1999): 28741-28750.
- 497 41 E. Zabránova, C. Matyska, L. Hanyk, and V. Palinkas. Constraints on the centroid moment tensors of
498 the 2010 maule and 2011 tohoku earthquakes from radial modes. *Geophysical Research Letters*, 39,
499 Sep 21 (2012). doi:10.1029/2012GL052850
- 500 42 S. Rosat, T. Sato, Y. Imanishi, J. Hinderer, Y. Tamura, H. McQueen, and M. Ohashi. High resolution
501 analysis of the gravest seismic normal modes after the 2004 mw=9 Sumatra earthquake using
502 superconducting gravimeter data. *Geophysical Research Letters*, 32(13), JUL 2005.
503 doi:10.1029/2005GL023128.
- 504 43 Wu, Ye, Shu Yang, and Liang Ding. "The Earth's Free Spherical Oscillations of the Chile
505 Earthquake." *Advanced Materials Research*. Vol. 622. Trans Tech Publications Ltd, 2013.
- 506 44 Beroza, Gregory C., and Thomas H. Jordan. "Searching for slow and silent earthquakes using free
507 oscillations." *Journal of Geophysical Research: Solid Earth* 95.B3 (1990): 2485-2510.
- 508 45 Derr, John S. "Internal structure of the earth inferred from free oscillations." *Journal of Geophysical*
509 *Research* 74.22 (1969): 5202-5220.
- 510 46 Dziewonski, A. M., and Freeman Gilbert. "Observations of normal modes from 84 recordings of the
511 Alaskan earthquake of 1964 March 28." *Geophysical Journal International* 27.4 (1972): 393-446.
- 512 47 Haddon, R. A. W., and K. E. Bullen. "An earth model incorporating free earth oscillation
513 data." *Physics of the Earth and Planetary Interiors* 2.1 (1969): 35-49.
- 514 48 Jordan, Thomas H., and Don L. Anderson. "Earth structure from free oscillations and travel
515 times." *Geophysical Journal International* 36.2 (1974): 411-459.
- 516 49 Lei, Xiang'E., Houze Xu, and Heping Sun. "Detection of spheroidal free oscillation excited by Peru
517 8.2 M s earthquake with five international superconducting gravimeter data." *Science in China Series*
518 *D: Earth Sciences* 48.1 (2005): 123-133.